Core-Shell Fe$_3$O$_4$@NCS-Mn Derived from Chitosan-Schiff Based Mn Complex with Enhanced Catalytic Activity for Oxygen Reduction Reaction

Jinhui Tong [1],*, Yuliang Li [1], Lili Bo [2], Wenhui Wang [1], Tao Li [1] and Qi Zhang [1]

[1] Key Laboratory of Eco-Environmental Polymer Materials of Gansu Province, Key Laboratory of Eco-Functional Polymer Materials of the Ministry of Education, College of Chemistry and Chemical Engineering, Northwest Normal University, Lanzhou 730070, China

[2] College of Science, Gansu Agricultural University, Lanzhou 730070, China

* Correspondence: jinhuitong@nwnu.edu.cn; Tel.: +86-931-7970806

check for updates

Abstract: A core-shell type of Fe$_3$O$_4$/NCS-Mn composite was prepared by pyrolyzing a precursor fabricated by coating a chitosan-Schiff base Mn complex on Fe$_3$O$_4$ cores. For comparison purposes, the Fe$_3$O$_4$@NCS sample in the absence of Mn and the Fe$_3$O$_4$@NC sample derived from just chitosan coating Fe$_3$O$_4$ were also prepared. Among the three catalysts, Fe$_3$O$_4$@NCS-Mn demonstrates the best electrocatalytic activity compared to commercial Pt/C (20%) for oxygen reduction reaction (ORR). The average of the transferred electron number (n) approached 3.6 in the range of −0.3 to −0.8 V (vs. Ag/AgCl). Moreover, the catalyst exhibited high stability and durability against methanol and may potentially be a promising ORR catalyst for fuel cells.

Keywords: chitosan Schiff base Mn complex; N-doped carbon; core-shell hybrids; oxygen reduction reaction

1. Introduction

Based on their paramount importance in electrochemical energy conversion and storage devices, it is essential to develop electrocatalysts with high efficiencies that minimize the overpotential in the oxygen reduction reaction (ORR) [1,2]. Although it is known to be efficient, the application of platinum-based catalysts is limited by scarcity, high cost, and poor durability against methanol [3]. Therefore, efforts have been made to develop Pt alternative catalysts for ORR. In alkaline media, electrocatalysts with various categories have been developed, further, the corresponding mechanisms have been explored, including nonmetal-doped carbon materials [4–8], carbon-transition metal hybrids [9–20], metal organic framework-modified nitrogen-doped graphene [21–23], and transition metal oxides [24–28]. Nonmetal heteroatom doped carbon materials and transition metal oxides have especially been given attention due to their advantages of high electron conductivity and favorable redox reversibility, respectively [29,30].

In our previous work, we developed several non-metallic heteroatom-doped carbon catalysts, including N-doped carbon spheres [31], porous N-doped carbon/carbon nanotube [32], N, S-doped graphitic carbon [33], and N, P dual-doped graphitic biocarbons [34]. The catalysts demonstrated comparable ORR activities and higher durability against methanol, especially when compared with commercial Pt/C (20%) in alkaline media [31–34]. Moreover, spinel transition metal oxides, such as Fe$_3$O$_4$ and their hybrids with nanocarbon materials, exhibited excellent catalytic activities in ORR [35–37]. While the spinel structure often provides two or more catalyst surfaces, it makes possible for the oxygen spill over reaction couple with the reaction path of ORR and therefore enhances the ORR catalytic activity [38].

Independent of the materials mentioned above, combining the virtues of the aforementioned various materials, we designed a core-shell structure of Fe_3O_4 cores coated with N-doped carbon-Mn shells derived from a chitosan Schiff-base Mn complex coating on Fe_3O_4 cores. In the present study, we expected an enhanced compositional homogeneity, catalytic activity, chemical stability, and methanol durability for ORR.

2. Results and Discussions

2.1. Catalysts Characterization

The X-ray diffraction (XRD) peaks at $2\theta \approx$ 30.1, 35.5, 44.6, 47.7, and 56.9° can be attributed to (220), (311), (200), (−210), and (333) plane of Fe_3O_4 (JCPDS No. 79-0418), respectively. The peak at $2\theta \approx$ 62.7, 65.0, and 75.6° can be attributed to the diffraction of Fe_2C (JCPDS No. 03-1022). The diffraction peaks at $2\theta \approx$ 41.3, 60.1, and 71.7° can be attributed to (201), (311), and (123) plane of $Fe_{2.7}Mn_{0.3}C$ (JCPDS No. 73-1341), respectively. The results confirm that Fe_2C and $Fe_{2.7}Mn_{0.3}C$ is formed by the reaction of Fe_3O_4 with the chitosan Schiff-base Mn (II) complex during the pyrolysis process. It is also clearly shown that the as-prepared catalysts are dominated by Fe_3O_4 (Figure 1).
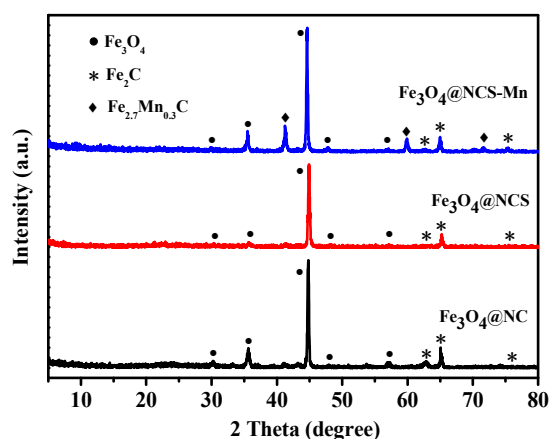

Figure 1. XRD patterns of Fe_3O_4@NC, Fe_3O_4@NCS, and Fe_3O_4@NCS-Mn catalysts.

The images of transmission electron microscope (TEM) in Figure 2 indicate a rather similar morphology between Fe_3O_4@NC and Fe_3O_4@NCS-Mn, with a size between 13–27 nm for the cores of Fe_3O_4 embedded in carbon shells. There were also certain aggregations of the particles of Fe_3O_4 likely caused by their magnetism. In Figure 3, scan electron microscope (SEM) image reveal a porous structure for the sample Fe_3O_4@NCS-Mn, which was potentially formed in the pyrolysis process due to the release of a large amount of gases during the carbonation of chitosan Schiff-base. The corresponding energy dispersive X-ray spectroscopy (EDS) images (based on the region of the yellow squared area of the SEM image) indicate that C, N, O, Mn, and Fe elements were evenly distributed in the sample.

The specific surface areas and pore size distributions were investigated using N_2 adsorption/desorption experiments for the three samples. As depicted in Figure 4, the samples exhibit type-II isotherms with H_4 hysteresis loop. This indicated the coexistence of slit-like pores as well as irregular mesoporous structure. The Brunauer-Emmett-Teller (BET) surface area/pore volume were 87/0.11, 214/0.28, and 143/0.17 $m^2 \cdot g^{-1}/cm^3 \cdot g^{-1}$ for Fe_3O_4@NC, Fe_3O_4@NCS, and Fe_3O_4@NCS-Mn, respectively (Table 1). Furthermore, all samples were dominated by the mesopores, which account for higher than 80% of BET surface areas and 71% for the samples' pore volumes (Table 1).
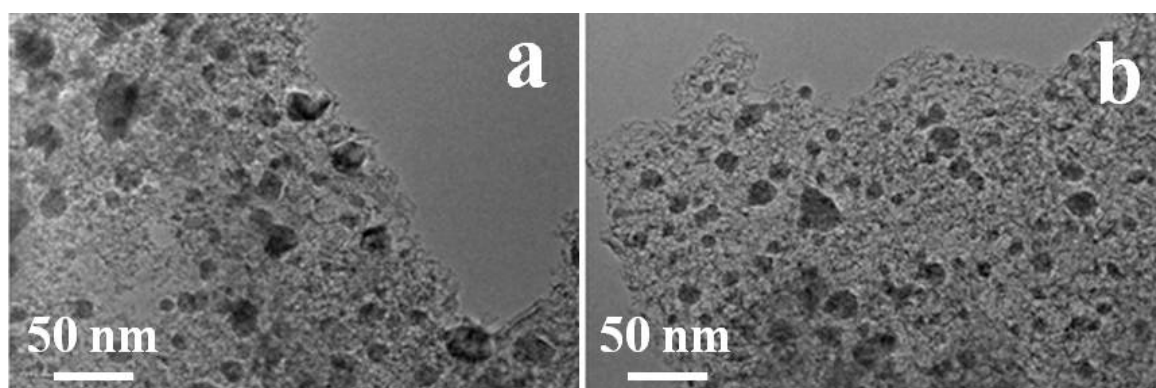
Figure 2. Typical TEM morphology of (**a**) Fe$_3$O$_4$@NC and (**b**) Fe$_3$O$_4$@NCS-Mn catalysts.

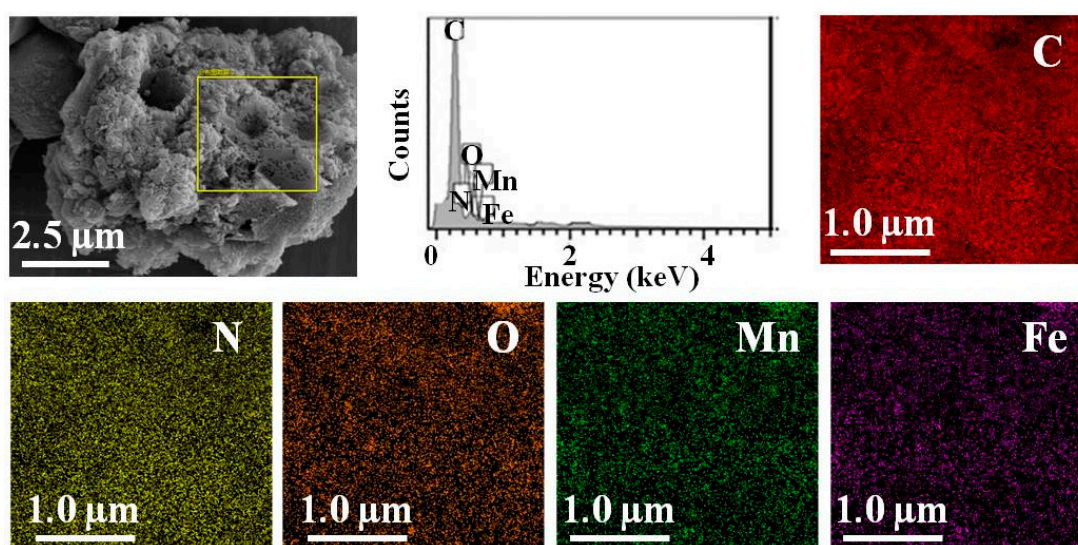**Figure 3.** SEM image of Fe$_3$O$_4$@NCS-Mn and corresponding EDS elemental mapping images of C, N, O, Mn, and Fe based on the selected region.

Table 1. The textural properties of Fe$_3$O$_4$@NC, Fe$_3$O$_4$@NCS, and Fe$_3$O$_4$@NCS-Mn.

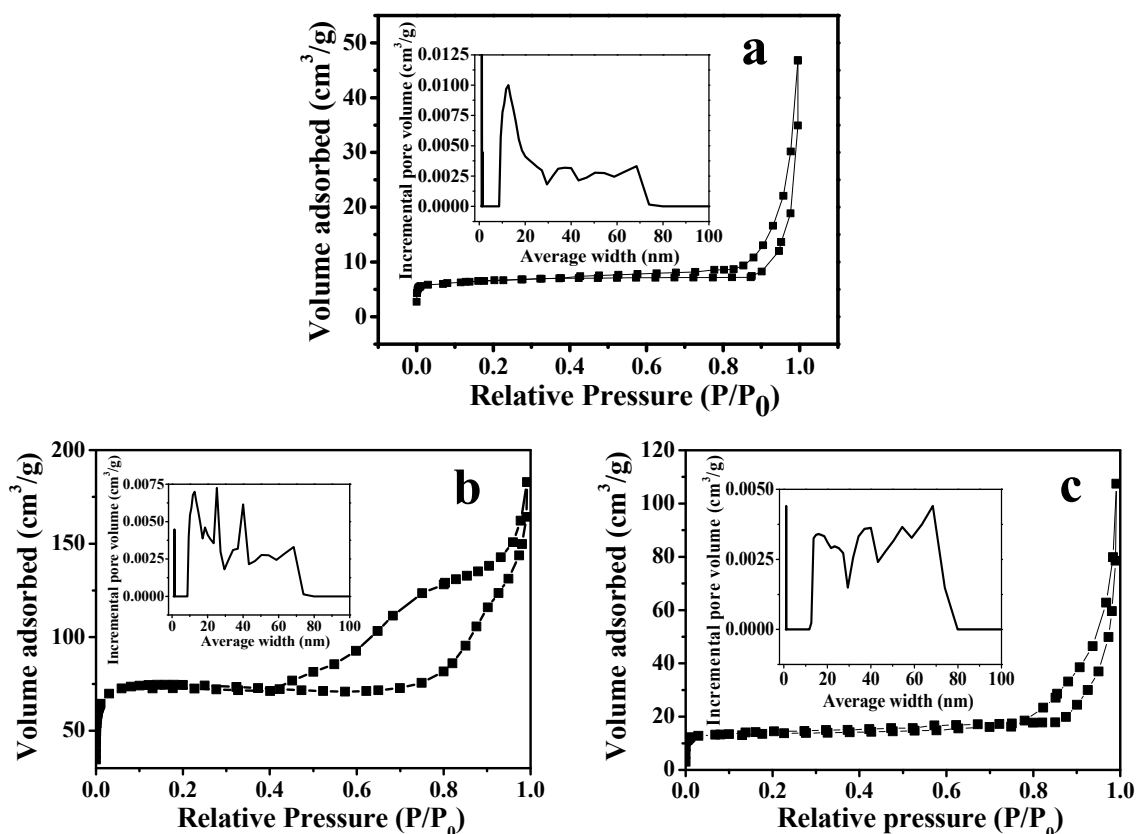| Sample		Fe$_3$O$_4$@NC	Fe$_3$O$_4$@NCS	Fe$_3$O$_4$@NCS-Mn
S$_{BET}$ [m^2·g^{-1}]	Total	87	214	143
	Microporous	17	36	21
	Mesoporous	70	178	122
Pore volume [cm^3·g^{-1}]	Total	0.11	0.28	0.17
	Microporous	0.03	0.05	0.02
	Mesoporous	0.08	0.23	0.15

Figure 4. N$_2$ adsorption/desorption isotherms and the corresponding pore size distribution curves of (**a**) Fe$_3$O$_4$@NC, (**b**) Fe$_3$O$_4$@NCS, and (**c**) Fe$_3$O$_4$@NCS-Mn.

2.2. Electrochemical Tests

The catalytic activities of the as-prepared catalysts for ORR were tested in O$_2$ saturated 0.1 M KOH. The commercial Pt/C (20 wt%) was used as a control catalyst. The linear sweep voltammetry (LSV) plots of different catalysts for ORR are displayed in Figure 5 and the characteristic parameters for ORR activity evaluation are listed in Table 2. As can be seen, the Fe$_3$O$_4$@NCS-Mn catalyst showed the highest onset potential and limiting current density of −0.02 V (vs. AgCl) and 3.8 mA/cm^2, which is almost the same with the corresponding ones of commercial Pt/C (20%). The catalyst also exhibited the most positive half-wave potential of −0.205 V (vs. AgCl), which is only 66 mV more negative than that of Pt/C (20%). The results confirm that the addition of Mn can enhance the catalytic activity.

The kinetics of ORR that employed Fe$_3$O$_4$@NCS-Mn as a catalyst were further investigated. The LSV curves at different rotation speeds are shown in Figure 6. As can be seen, the limiting current density increased with the increase in the rotating speeds due to the enhanced oxygen flux to the electrode surface [38]. Figure 7a shows the plots of j^{-1} versus $\omega^{-1/2}$ at different potentials in the range of −0.3~−0.55 V. A great linear correlation between j^{-1} and $\omega^{-1/2}$ confirms that the reaction is first-order with regard to the concentration of dissolved oxygen. Based on the Koutecky-Levich (K-L) equation, Figure 7b presents the transferred electron number (*n*) in ORR under different potentials. The average *n* was found to be 3.6 in the potential range of −0.30 V to −0.60 V, which indicates an approximate 4e$^-$ ORR process. This is considered to be the most efficient ORR pathway.
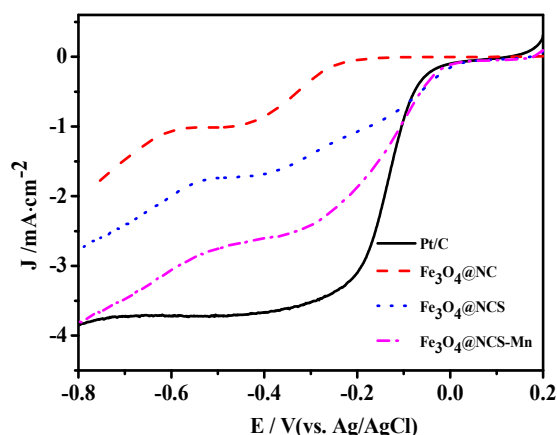
Figure 5. Polarization curves of Pt/C (20%), Fe_3O_4@NC, Fe_3O_4@NCS, and Fe_3O_4@NCS-Mn. Scan rate: 10 mV·s^{-1}; rotation speed: 1600 rpm.

Table 2. Comparison of catalytic activity of the catalysts towards oxygen reduction reaction (ORR).

Sample	Onset Potential (V vs. Ag/AgCl)	Half-Wave Potential (V vs. Ag/AgCl)	Limiting Current Density (mA·cm^{-2})
Pt/C	−0.02	−0.139	3.8
Fe_3O_4@NC	−0.21	−0.561	2.0
Fe_3O_4@NCS	−0.02	−0.292	2.8
Fe_3O_4@NCS-Mn	−0.02	−0.205	3.8
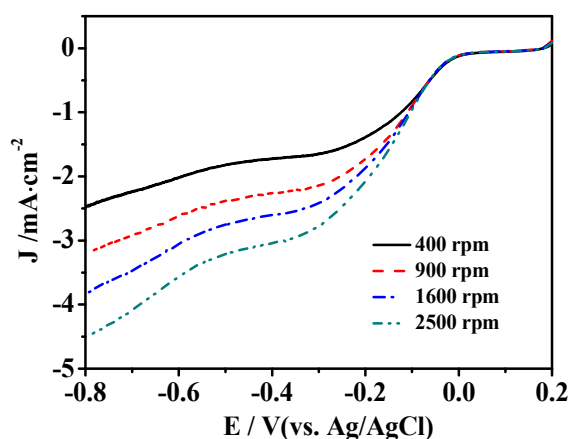
Figure 6. Polarization curves of Fe_3O_4@NCS-Mn catalyst at different rotation speeds. Scan rate: 10 mV·s^{-1}.

In methanol-based fuel cells, one important feature for ORR catalyst is its durability and tolerance toward methanol. The durability of Fe_3O_4@NCS-Mn against methanol was tested using cyclic voltammetry (CV) measurements. Figure 8a indicates that there was no significant change in the CV curve upon the addition of 3 M CH_3OH to O_2 saturated 0.1 M KOH, except for a slight decrease in reduction current and peak potential. Within the entire scanning range, there was no observable current for the oxidation of methanol. Comparatively, CV curve for Pt/C (20%) electrode shows a peak identified as the oxidation current of methanol, and the O_2 reduction peak completely disappeared under the same conditions (Figure 8b). Therefore, Fe_3O_4@NCS-Mn is a more selective ORR catalyst than Pt/C (20%) with much stronger durability against methanol.
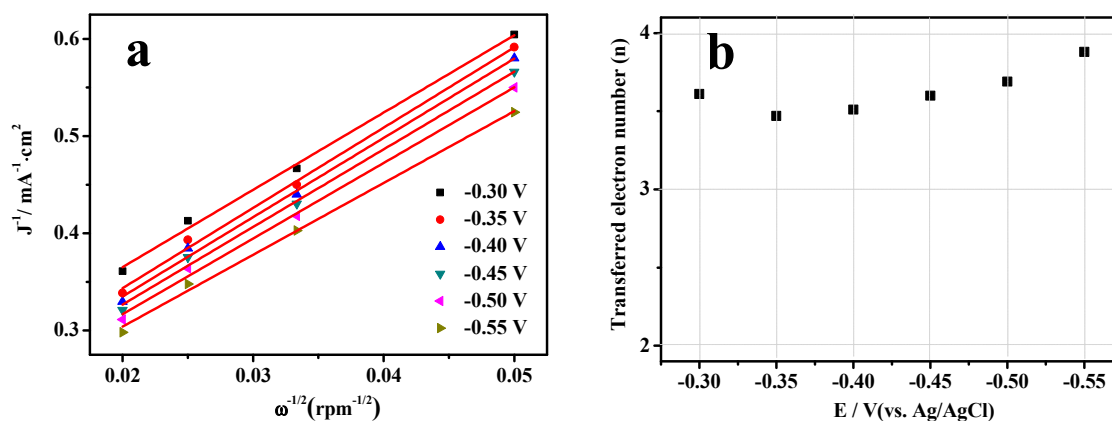
Figure 7. (**a**) Koutecky-Levich (K-L) plots of Fe_3O_4@NCS-Mn catalyst for ORR; (**b**) the dependence of the transferred electron number (*n*) on the potential.
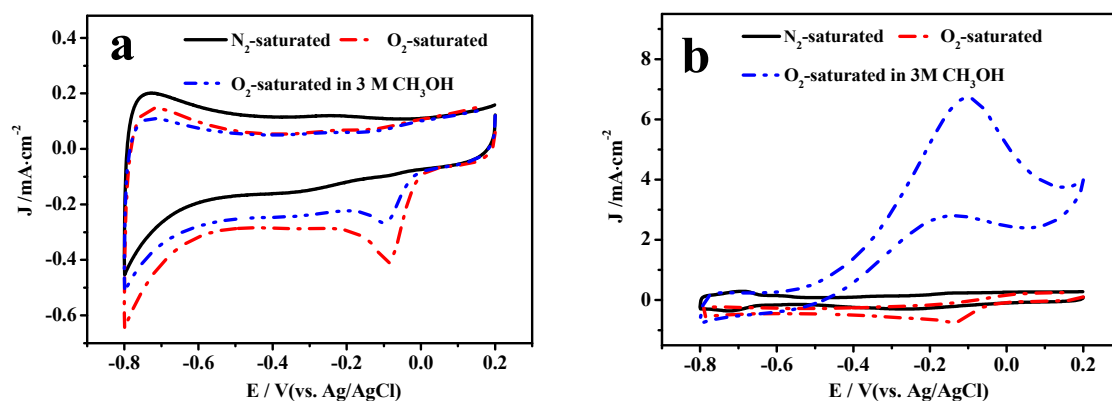

Figure 8. CV curves of (**a**) Fe_3O_4@NCS-Mn and (**b**) Pt/C (20%) in N_2 or O_2-saturated 0.1 M KOH as well as O_2-saturated 0.1 M KOH with 3 M CH_3OH. Scan rate: 10 mV·s^{-1}.

The traditional ORR catalysts have been challenged in their stabilities, which is another important feature for ORR catalyst with great quality. The relative current was measured for both Fe_3O_4@NCS-Mn and commercial Pt/C (20%) at −0.3 V (vs. Ag/AgCl) in an O_2 saturated 0.1 M KOH solution. Figure 9 indicates that the relative current of Fe_3O_4@NCS-Mn shows a decay of 53.2%, whereas the Pt/C (20%) catalyst exhibits a decay of 58.5% after a 36,000 s chronoamperometric test. Therefore, Fe_3O_4@NCS-Mn is more stable than the Pt/C (20%) catalyst in the alkaline medium.

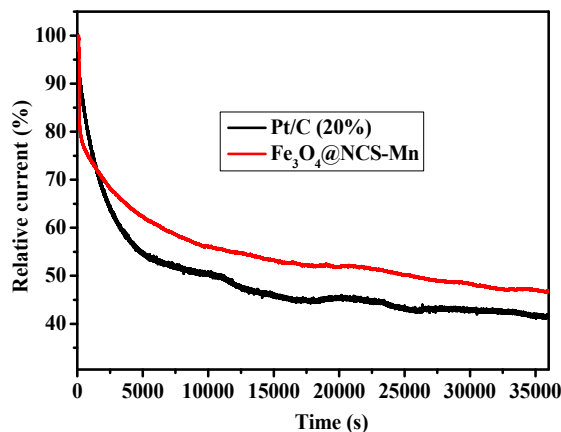**Figure 9.** The chronoamperometric current-time curves of Pt/C (20%) and Fe_3O_4@NCS-Mn catalyst for 36,000 s. Rotation speed: 1600 rpm.

3. Experimental Methods

3.1. Materials and Instruments

Iron(II) chloride tetrahydrate, chitosan, salicylaldehyde and manganese nitrate (50 wt% aqueous solution) were supplied by Sinopharm Chemical Reagent Co. Ltd (Shanghai, China). Pt/C (20 wt% Pt on carbon black) and Nafion (5 wt%) were supplied by Alfa Aesar (Haverhill, MA, USA). All reagents were of analytical grade and were used as received. A field-emission scanning electron microscope (JSM-6701F, FEOL, Japan), a transmission electron microscope (JEM-2010, Japan), a XRD-6000 diffractometer with Cu Kα radiation (λ = 1.54178 Å) (Shimadzu, Japan) and an ASAP2020 Micromeritics Instrument (TriStar II, USA) were used for characterization of the catalysts. A 760E electrochemical workstation (CH Instruments, Shanghai, China) was used for electrochemistry tests.

3.2. Preparation of the Catalysts

The Fe_3O_4@chitosan Schiff-base Mn (II) complex was prepared as described in our previous work [39]. The catalyst Core-shell Fe_3O_4@NCS-Mn was prepared by pyrolyzing Fe_3O_4@chitosan Schiff-base Mn (II) complex at 800 °C in N_2 for 2 h with a heating rate of 5 °C/min. For comparison purpose, the other two catalysts were derived from different precursors and also prepared under the same conditions. One was derived from the precursor of Fe_3O_4@chitosan (denoted as Fe_3O_4@NC), while the other was derived from the precursor of Fe_3O_4@chitosan Schiff-base in the absence of Mn (denoted as Fe_3O_4@NCS).

3.3. Electrochemistry Tests

The electrocatalytic performances of the as-prepared samples were tested on the electrochemical workstation using an Ag/AgCl (in 3 M KCl) as the reference electrode and a graphite rod as the counter electrode and a 3 mm glassy carbon as the working electrode. A catalyst suspension to be tested was prepared using ultrasonically dispersed 2.5 mg of the catalyst into a mixture solvent of 980 μL ethanol and 20 μL water. The electrode to be tested was prepared by depositing 7 μL of the above suspension onto the working electrode and dried at 40 °C for 2 h with a catalyst loading of 0.25 mg·cm^{-2}. Before the test, the electrolyte solution was saturated using O_2. The working electrode was activated using the cyclic voltammetry (CV) method at 50 mV·s^{-1} for several cycles.

4. Conclusions

Combining the advantages of transition metal oxide and nitrogen-doped carbon material, the present work developed a feasible strategy to synthesize a core-shell structure based on a chitosan-Schiff base Mn complex coating on Fe_3O_4 cores (Fe_3O_4@NC-Mn). Used as the ORR catalyst, Fe_3O_4@NCS-Mn achieved nearly equivalent onset potential and maximum current density to the commercial Pt/C (20%) catalyst. Moreover, it demonstrated impressive chemical stability and stronger durability against methanol. Along with an average number of the transferred electron of 3.6, Fe_3O_4@NCS-Mn can be potentially used as the ORR catalyst in methanol based fuel cell.

References

1. Chen, X.; Li, C.; Graetzel, M.; Kostecki, R.; Mao, S.S. Nanomaterials for renewable energy production and storage. *Chem. Soc. Rev.* **2012**, *41*, 7909–7937. [CrossRef] [PubMed]

2. Guo, Y.G.; Hu, J.S.; Wan, L.J. Nanostructured materials for electrochemical energy conversion and storage devices. *Adv. Mater.* **2008**, *20*, 2878–2887. [CrossRef]

3. Zhang, L.; Zhang, J.; Wilkinson, D.P.; Wang, H. Progress in preparation of non-noble electrocatalysts for PEM fuel cell reactions. *J. Power Sources* **2006**, *156*, 171–182. [CrossRef]

4. Wang, B. Recent development of non-platinum catalysts for oxygen reduction reaction. *J. Power Sources* **2005**, *152*, 1–15. [CrossRef]

5. Wang, R.; Zhou, T.; Li, H.; Wang, H.; Feng, H.; Goh, J.; Ji, S. Nitrogen-rich mesoporous carbon derived from melamine with high electrocatalytic performance for oxygen reduction reaction. *J. Power Sources* **2014**, *261*, 238–244. [CrossRef]

6. Wang, S.; Yu, D.; Dai, L. Polyelectrolyte functionalized carbon nanotubes as efficient metal-free electrocatalysts for oxygen reduction. *J. Am. Chem. Soc.* **2011**, *133*, 5182–5185. [CrossRef]

7. Zhuang, S.; Nunna, B.B.; Boscoboinik, J.A.; Lee, E.S. Nitrogen-doped graphene catalysts: High energy wet ball milling synthesis and characterizations of functional groups and particle size variation with time and speed. *Int. J. Energy Res.* **2017**, *41*, 2535–2554. [CrossRef]

8. Zhuang, S.; Lee, E.S.; Lei, L.; Nunna, B.B.; Kuang, L.; Zhang, W. Synthesis of nitrogen-doped graphene catalyst by high-energy wet ball milling for electrochemical systems. *Int. J. Energy Res.* **2016**, *40*, 2136–2149. [CrossRef]

9. Li, Z.; Li, G.; Jiang, L.; Li, J.; Sun, G.; Xia, C.; Li, F. Ionic liquids as precursors for efficient mesoporous iron-nitrogen-doped oxygen reduction electrocatalysts. *Angew. Chem. Int. Ed.* **2015**, *54*, 1494–1498. [CrossRef]

10. Lin, L.; Zhu, Q.; Xu, A.W. Noble-metal-free Fe-N/C catalyst for highly efficient oxygen reduction reaction under both alkaline and acidic conditions. *J. Am. Chem. Soc.* **2014**, *136*, 11027–11033. [CrossRef]

11. Wen, Z.; Ci, S.; Zhang, F.; Feng, X.; Cui, S.; Mao, S.; Luo, S.; He, Z.; Chen, J. Nitrogen-enriched core-shell structured Fe/Fe$_3$C-C nanorods as advanced electrocatalysts for oxygen reduction reaction. *Adv. Mater.* **2012**, *24*, 1399–1404. [CrossRef] [PubMed]

12. Liu, Y.; Li, T.; Cao, X.; Liu, J.; Zhang, J.; Jia, J.; Wang, F.; Pan, K. Electrospun Fe$_2$C-loaded carbon nanofibers as efficient electrocatalysts for oxygen reduction reaction. *Nanotechnology* **2019**, *30*, 325403. [CrossRef] [PubMed]

13. Sabhapathy, P.; Liao, C.C.; Chen, W.-F.; Chou, T.C.; Shown, I.; Sabbah, A.; Lin, Y.G.; Lee, J.F.; Tsai, M.K.; Chen, K.H.; et al. Highly efficient nitrogen and carbon coordinated N-Co-C electrocatalysts on reduced graphene oxide derived from vitamin-B$_{12}$ for the hydrogen evolution reaction. *J. Mater. Chem. A* **2019**, *7*, 7179–7185. [CrossRef]

14. Song, L.; Wang, T.; Li, L.; Wu, C.; He, J. Zn$_3$[Fe(CN)$_6$)]$_2$ derived Fe/Fe$_5$C$_2$@N-doped carbon as a highly effective oxygen reduction reaction catalyst for zinc-air battery. *Appl. Catal. B Environ.* **2019**, *244*, 197–205. [CrossRef]

15. Tang, Y.; Lan, K.; Li, F.; Jiang, P.; Wang, X.; Yang, Y.; Gao, W.; Wang, B.; Li, R. Reduced graphene oxide-supported Ni-Mo$_x$C electrocatalyst for hydrogen evolution reaction prepared by ultrasonication and lyophilization. *Int. J. Hydrog. Energy* **2019**, *44*, 9328–9337. [CrossRef]

16. Zhang, N.; Cao, L.; Feng, L.; Huang, J.; Kajiyoshi, K.; Li, C.; Liu, Q.; Yang, D.; He, J. Co, N-Codoped porous vanadium nitride nanoplates as superior bifunctional electrocatalysts for hydrogen evolution and oxygen reduction reactions. *Nanoscale* **2019**, *11*, 11542–11549. [CrossRef] [PubMed]

17. Zhang, X.; Mollamahale, Y.B.; Lyu, D.; Liang, L.; Yu, F.; Qing, M.; Du, Y.; Zhang, X.; Tian, Z.Q.; Shen, P.K. Molecular-level design of Fe-N-C catalysts derived from Fe-dual pyridine coordination complexes for highly efficient oxygen reduction. *J. Catal.* **2019**, *372*, 245–257. [CrossRef]

18. Lo Vecchio, C.; Sebastian, D.; Lazaro, M.J.; Arico, A.S.; Baglio, V. Methanol-tolerant M-N-C catalysts for oxygen reduction reactions in acidic media and their application in direct methanol fuel cells. *Catalysts* **2018**, *8*, 650. [CrossRef]

19. Qiao, X.; Jin, J.; Fan, H.; Cui, L.; Ji, S.; Li, Y.; Liao, S. Cobalt and nitrogen co-doped graphene-carbon nanotube aerogel as an efficient bifunctional electrocatalyst for oxygen reduction and evolution reactions. *Catalysts* **2018**, *8*, 275. [CrossRef]

20. Wu, Y.; Li, Y.; Mao, J.; Wu, H.; Wu, T.; Li, Y.; Zeng, B.; Xu, Y.; Yuan, C.; Dai, L. Metallosupramolecular polymer precursor design for multi-element co-doped carbon shells with improved oxygen reduction reaction catalytic activity. *Catalysts* **2019**, *9*, 102. [CrossRef]

21. Zhuang, S.; Nunna, B.B.; Lee, E.S. Metal organic framework-modified nitrogen-doped graphene oxygen reduction reaction catalyst synthesized by nanoscale high-energy wet ball-milling structural and electrochemical characterization. *MRS Commun.* **2018**, *8*, 40–48. [CrossRef]

22. Zhuang, S.; Singh, H.; Nunna, B.B.; Mandal, D.; Boscoboinik, J.A.; Lee, E.S. Nitrogen-doped graphene-based catalyst with metal-reduced organic framework: Chemical analysis and structure control. *Carbon* **2018**, *139*, 933–944. [CrossRef]

23. Singh, H.; Zhuang, S.; Nunna, B.B.; Lee, E.S. Thermal stability and potential cycling durability of nitrogen-doped graphene modified by metal-organic framework for oxygen reduction reactions. *Catalysts* **2018**, *8*, 607. [CrossRef]

24. Ashok, A.; Kumar, A.; Ponraj, J.; Mansour, S.A.; Tarlochan, F. Highly active and stable bi-functional NiCoO$_2$ catalyst for oxygen reduction and oxygen evolution reactions in alkaline medium. *Int. J. Hydrog. Energy* **2019**, *44*, 16603–16614. [CrossRef]

25. Huang, K.; Liu, J.; Wang, L.; Chang, G.; Wang, R.; Lei, M.; Wang, Y.; He, Y. Mixed valence CoCuMnO$_x$ spinel nanoparticles by sacrificial template method with enhanced ORR performance. *Appl. Surf. Sci.* **2019**, *487*, 1145–1151. [CrossRef]

26. Li, Z.; Li, B.; Chen, J.; Pang, Q.; Shen, P. Spinel NiCo$_2$O$_4$ 3D nanoflowers supported on graphene nanosheets as efficient electrocatalyst for oxygen evolution reaction. *Int. J. Hydrog. Energy* **2019**, *44*, 16120–16131. [CrossRef]

27. Shen, Y.; Guo, S.G.; Du, F.; Yuan, X.B.; Zhang, Y.; Hu, J.; Shen, Q.; Luo, W.; Alsaedi, A.; Hayat, T.; et al. Prussian blue analogue-derived Ni and Co bimetallic oxide nanoplate arrays block-built from porous and hollow nanocubes for the efficient oxygen evolution reaction. *Nanoscale* **2019**, *11*, 11765–11773. [CrossRef]

28. Yan, S.; Xue, Y.; Li, S.; Shao, G.; Liu, Z. Enhanced bifunctional catalytic activity of manganese oxide/perovskite hierarchical core-shell materials by adjusting the interface for metal-air batteries. *ACS Appl. Mater. Interface* **2019**, *11*, 25870–25881. [CrossRef]

29. Han, X.; Zheng, Z.; Chen, J.; Xue, Y.; Li, H.; Zheng, J.; Xie, Z.; Kuang, Q.; Zheng, L. Efficient oxygen reduction on sandwich-like metal@N-C composites with ultrafine Fe nanoparticles embedded in N-doped carbon nanotubes grafted on graphene sheets. *Nanoscale* **2019**, *11*, 12610–12618. [CrossRef]

30. Paulraj, A.R.; Kiros, Y.; Gothelid, M.; Johansson, M.B. NiFeO$_x$ as a bifunctional electrocatalyst for oxygen reduction (OR) and evolution (OE) reaction in alkaline media. *Catalysts* **2018**, *8*, 328. [CrossRef]

31. Tong, J.; Li, W.; Bo, L.; Wang, W.; Li, Y.; Li, T.; Zhang, Q.; Fan, H. Simple synthesis of nitrogen-doped carbon spheres as a highly efficient metal-free electrocatalyst for the oxygen reduction reaction. *Chin. J. Catal.* **2018**, *39*, 1138–1145. [CrossRef]

32. Tong, J.; Li, W.; Bo, L.; Ma, J.; Li, T.; Li, Y.; Zhang, Q.; Fan, H. Composite of hierarchically porous N-doped carbon/carbon nanotube with greatly improved catalytic performance for oxygen reduction reaction. *ACS Sustain. Chem. Eng.* **2018**, *6*, 8383–8391. [CrossRef]

33. Tong, J.; Li, W.; Ma, J.; Wang, W.; Bo, L.; Lei, Z.; Mahboob, A. Nitrogen and sulfur dual self-doped graphitic carbon with highly catalytic activity for oxygen reduction reaction. *ACS Appl. Energy Mater.* **2018**, *1*, 5746–5754. [CrossRef]

34. Tong, J.; Ma, W.; Wang, W.; Ma, J.; Li, W.; Bo, L.; Fan, H. Nitrogen/phosphorus dual-doped hierarchically porous graphitic biocarbon with greatly improved performance on oxygen reduction reaction in alkaline media. *J. Electroanal. Chem.* **2018**, *809*, 163–170. [CrossRef]

35. Wu, Z.S.; Yang, S.; Sun, Y.; Parvez, K.; Feng, X.; Mullen, K. 3D nitrogen-doped graphene aerogel-supported Fe$_3$O$_4$ nanoparticles as efficient electrocatalysts for the oxygen reduction reaction. *J Am. Chem. Soc.* **2012**, *134*, 9082–9085. [CrossRef] [PubMed]

36. Su, Y.H.; Jiang, H.L.; Zhu, Y.H.; Yang, X.L.; Shen, J.H.; Zou, W.J.; Chen, J.D.; Li, C.Z. Enriched graphitic N-doped carbon-supported Fe$_3$O$_4$ nanoparticles as efficient electrocatalysts for oxygen reduction reaction. *J. Mater. Chem. A* **2014**, *2*, 7281–7287. [CrossRef]

37. Barros, W.R.P.; Wei, Q.; Zhang, G.; Sun, S.; Lanza, M.R.V.; Tavares, A.C. Oxygen reduction to hydrogen peroxide on Fe$_3$O$_4$ nanoparticles supported on Printex carbon and graphene. *Electrochim. Acta* **2015**, *162*, 263–270. [CrossRef]

38.　Liu, J.; Liu, J.; Song, W.; Wang, F.; Song, Y. The role of electronic interaction in the use of Ag and Mn_3O_4 hybrid nanocrystals covalently coupled with carbon as advanced oxygen reduction electrocatalysts. *J. Mater. Chem. A* **2014**, *2*, 17477–17488. [CrossRef]

39.　Cai, X.; Wang, H.; Zhang, Q.; Tong, J.; Lei, Z. Magnetically recyclable core-shell Fe_3O_4@chitosan-Schiff base complexes as efficient catalysts for aerobic oxidation of cyclohexene under mild conditions. *J. Mol. Catal. A Chem.* **2014**, *383*, 217–224. [CrossRef]